Revisiting the Crystal Structure of Layered Oxychalcogenides Ln2O2S2 (Ln = La, Pr, and Nd)

Louis-Béni Mvélé, Shunsuke Sasaki, Camille Latouche, Philippe Deniard, Etienne Janod, Isabelle Braems, Stéphane Jobic, Laurent Cario

Revisiting the crystal structure of layered oxychalcogenides $Ln_2O_2S_2$ (*Ln* = La, Pr, Nd)

Louis-Béni Mvélé, Shunsuke Sasaki, Camille Latouche, Philippe Deniard, Etienne Janod, Isabelle Braems, Stéphane Jobic, Laurent Cario**

[1] Nantes Université, CNRS, Institut des Matériaux de Nantes Jean Rouxel, IMN, F-44000 Nantes, France

KEYWORDS. oxysulfide; sulfur dimers; crystal disorder; Raman spectroscopy of S−S bonds.

ABSTRACT.

$La_2O_2S_2$ was recently used as a precursor to prepare either a new metastable form of La_2O_2S by de-insertion of half sulfur atoms of (S_2) dimers or quaternary compounds by insertion of a coinage metal (e.g. $La_2O_2Cu_2S_2$). A strong structural filiation exists between the polysulfide precursor and the synthesized products, which highlights the topochemical nature of these reactions. Nevertheless, the crystal structure of the precursor material is still a matter of debate. Namely, several structural models were reported so far in the literature with different space groups and/or crystal systems. All these models are built upon on infinite [Ln_2O_2] slabs separated from each other by a flat sulfur layer of (S_2) dumbbells. Nevertheless, all (S_2) dimers within a given sulfur layer may rotate in phase by 90° compared to the ideal model that induces an overall atomic disorder in (S_2) dimers orientation along the stacking axis. This leads to some *imbroglio* and much confusion in the description of structural arrangement of $Ln_2O_2S_2$ materials. Here the crystal structures of $La_2O_2S_2$ and its Pr and Nd variants are revisited. We propose an alternative model that reconciles pre-existing structural descriptions of $Ln_2O_2S_2$ (*Ln* = La, Pr, Nd) materials and highlights the strong dependency of the degree of long-range ordering of the sulfur layers with the synthesis conditions.

INTRODUCTION

Transition metal and lanthanides chalcogenides as well as oxy-chalcogenides belong to a broad range of materials studied for modern technological applications such as nonlinear optics, [1] bioimaging,[2,3] thermoelectric energy conversion,[4] photocatalysis,[5] unconventional superconductivity,[6] complex magnetism, [7,8] etc. We have recently proposed a novel soft chemistry route to prepare metastable materials.[9] The synthetic strategy is based on the redox reactivity of $(Q_n)^{2-}$ (Q= S, Se; n= 2, 3 or 4) oligomers towards reductant species in the solid state. In that context, we have demonstrated that $(S_2)^{2-}$ dimer embedded in the $La_2O_2S_2$ precursor undergoes a redox reaction with zerovalent metals. This reaction leads either to the intercalation of the metal cations or to the deintercalation of sulfur anions.[10,11] In both cases, the structural integrity of infinite $[La_2O_2]^{2+}$ layers are maintained while sulfur atoms are reorganized within their 2D array to give rise to different structural blocks.

According to the topochemical nature of the reactions mentioned above, they should be discussed on the basis of a firm understanding of the precursor structure, including pre-existing intrinsic disorder for instance. However the exact structure of $La_2O_2S_2$ material and its Pr and Nd derivatives is still subject to debate. Mainly, two models confront each other. Both describe the materials as built upon fluorite-type $[La_2O_2]^{2+}$ slabs and 2D arrays of $(S_2)^{2-}$ dimers that continuously alternate along the stacking axis. The main difference lies in the (dis-)ordering of S atoms within sulfur layers or between sulfur layers.

In this study, we revisit the crystal structure of $Ln_2O_2S_2$ (*Ln*= La, Pr, and Nd) materials and propose an alternative model to the one of Ostéro and Leblanc (perfect long-range stacking of unfaulted sulfur layers)[11] and the one of Ballestracci [12] (randomly stacking of possibly faulted S-layers). This “hybrid” model, that reconciles the two points of view, was employed to perform

Rietveld analyses of $Ln_2O_2S_2$ (*Ln* = La, Pr and Nd) synthesized in different conditions. It allowed us to discuss how different synthetic conditions as well as the chemical nature of the rare-earth may affect the degree of disorder. Furthermore, computational analyses of Raman spectra collected on $La_2O_2S_2$ samples evidence definitely the complete ordering of sulfur atoms within a 2D sulfur array and corroborate our narrative that the observed disorder in sulfur layers originates only from orientational faults of S-layers all along the stacking axis.

EXPERIMENTAL SECTION

Synthesis. $La_2O_2S_2$ was prepared via four different chemical routes. **Method 1**. La_2O_3 (1398.2 mg, powder from Aldrich 99.9%), La (596.5 mg, ingot from alpha Aesar 99.9%) and S (412.82 mg, powder from Aldrich 99.99%) powders were weighted in the 2:2:6 molar ratio, mixed and ground altogether in an agate mortar. The blend was then placed in a carbon coated silica tube, flame-sealed under vacuum, and heated in a furnace at 650 °C for 72 h (heating and cooling rates of 50 °C/h and 100 °C/h). **Method 2**. Homemade La_2O_2S (hexagonal form, 500 mg) and sulfur (56.27 mg) were mixed altogether in a 1:1.2 molecular ratio and heated in an evacuated silica tube in the same conditions as method 1. For both methods, repetitive thermal treatments in the same conditions with addition of sulfur were needed to get pure materials. **Method 3**. Method 3 was similar to method 2 where stable La_2O_2S (*hP*-La_2O_2S) was replaced by metastable La_2O_2S (*oA*-La_2O_2S) prepared as reported by Sasaki *et al.*[9]. *oA*-Ln_2O_2S and S were weighted in the 1:1.2 molar ratio and heated at 200°C for 24 h. **Method 4**. $La_2O_2Cu_2S_2$ precursor was synthesized as reported by Sasaki *et al.*[10] Oxidative deintercalation of $La_2O_2Cu_2S_2$ (100 mg) in presence of iodine (55.7 mg, Alpha Aesar 99.99%) (1:1.1 $La_2O_2Cu_2S_2$:I_2 ratio) was carried out in evacuated silica tube at 200°C for 24h. CuI by-product was eliminated by washing with dry acetonitrile. $La_2O_2S_2$ synthesized using methods 1 to 4 are hereafter labeled $La_2O_2S_2$-1, $La_2O_2S_2$-2, $La_2O_2S_2$-3

and $La_2O_2S_2$-4, respectively. $Pr_2O_2S_2$ and $Nd_2O_2S_2$ compounds were only synthesized via the method 1 (same temperature but longer plateau of 120 h) and will be referenced as $Pr_2O_2S_2$-1 and $Nd_2O_2S_2$-1 hereafter. The following precursors Pr_2O_3 (1396.25 mg, powder from Aldrich 99.9%), Pr (596,52 mg, ingot from Alpha Aesar 99.9%) and S (407.26 mg, powder from Aldrich 99.99%) were used to synthesize $Pr_2O_2S_2$; Nd_2O_3 (545.87 mg, powder from Aldrich 99.9%), Nd (235 mg, ingot from Alpha Aesar 99.9%) and S (156.05 mg, powder from Aldrich 99.99%) were used to synthesize $Nd_2O_2S_2$.

X-ray diffraction. Powder X-ray diffraction was carried out at room temperature on a Bruker D8 Advance diffractometer (Bragg−Brentano, θ−2θ) equipped with a Lynxeye position-sensitive detector and a copper anticathode. The powder patterns were collected at room temperature from 10 to 90° in 2θ with a step of 0.009 ° (λ = 1.540598 Å). The powder patterns were refined with the Jana 2006 chain program. [13]

Chemical analyses. Powders were embedded in epoxy, and as-prepared composites were polished to get flat surfaces. Elemental analyses were performed with an Energy Dispersive X-ray spectrometer (JEOL 5800 LV equipped with a SAMx SDD detector) at 20 KeV. The use of calibrated internal standards (Al_2O_3, FeS_2, LaB_6, PrF_3 and NdF_3) leads to the reproducible La/O/S 32.78/33.51/33.71, Pr/O/S 34.95/33.02/32.04 and Nd/O/S 32.58/34.17/33.25 atomic ratios in good agreement with the $Ln_2O_2S_2$ chemical compositions.

Raman spectroscopy. Raman spectra were collected on $La_2O_2S_2$-1, $Pr_2O_2S_2$-1 and $Nd_2O_2S_2$-1 powders in backscattered geometry mode using a Renishaw spectrometer equipped with a 514 nm laser. The power of this latter was maintained at 0.15 mW. Two measurements (at least) were carried out at different points of each samples to check their chemical homogeneity.

UV-vis absorption spectroscopy. Diffuse reflectance spectra on powdered samples were measured using a Varian Cary 5G spectrophotometer equipped with a 60 mm-∅ integrating sphere.

Computational investigations. Computations were performed using hybrid functionals on the orthorhombic $La_2O_2S_2$ material using the CRYSTAL17 and the VASP packages [14] for the vibrational properties and electronic properties, respectively (See SI for further details).

RESULTS AND DISCUSSION

Several crystal data were reported in the literature for $La_2O_2S_2$, $Pr_2O_2S_2$ and $Nd_2O_2S_2$ over the years (see lists in Table S1). The discrepancy between the proposed models originates from the difficulty to discriminate between an orthorhombic cell and its (pseudo-)tetragonal variant, and subsequently between an orthorhombic and a tetragonal symmetry of the overall structural arrangement. As a matter of fact, two parameters of the orthorhombic cell are almost identical and are not distinguishable within the estimated standard deviations in studied samples.

The structural description of $La_2O_2S_2$ using the orthorhombic setting with space group *Cmc*a, (renamed hereafter *Cmce* to respect the IUPAC recommendations[15]) is the most recent. It was obtained by Ostoréro et Leblanc[11] from a single crystal X-ray analysis. The model considers three unique and distinct atomic positions for *Ln*, O and S atoms, and the resulting $Ln_2O_2S_2$ structure can be regarded as built upon infinite $[Ln_2O_2]^{2+}$ slabs separated from each other by a flat sulfur layer consisting of $(S_2)^{2-}$ dumbbells lying on the mirror plane (see Fig. 1a and Fig. S1 in supplementary information for the atomic environments). The structure of the oxide slabs is commonly referred to as fluorite type by analogy with the (001) $[Ca_2F_2]$ blocks of the CaF_2 fluorine structure where calcium (fluorine) atoms are replaced by oxygen (lanthanide) ones.

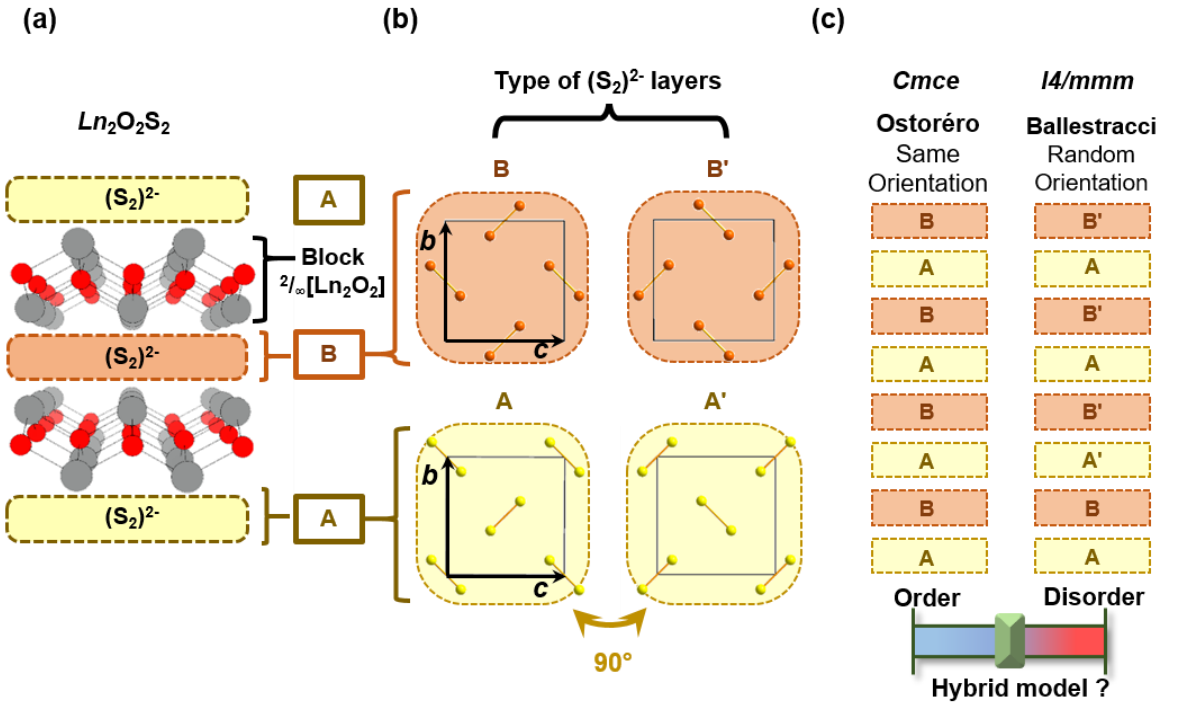

Figure 1. (a) Generic description of the structures of $Ln_2O_2S_2$ (*Ln* = La, Pr and Nd), where $[Ln_2O_2]^{2+}$ fluorite layers stack with 2D array of $(S_2)^{2-}$ dimers. (b) Representation of the four different possible arrangements for packing of $(S_2)^{2-}$ dimers within each 2D array. Only layers A and B are present in the Ostoréro and Leblanc model [11]. They are related by a a/2 + b/2 translation of the *Cmce* SG. Layers A and B, and A' and B' are observed in Ballestracci model [12]. Layers A and A', and B and B' are related by a 90° rotation (pseudo 4-fold axis) along the stacking axis. Layers A and A', and B and B' are represented by yellow and orange boxes, respectively. (c) Schematic representations of the stacking of Sulfur layers in the Ostoréro and Leblanc model (Cmnce SG) (left) and the Bellestraci model (*I4/mmm* SG) (right) where layers A (B) are randomly replaced by layers A' (B'), and A (B) and A' (B') layers being equiprobable. The hybrid model would correspond to a situation where layers A and B are replaced partially by layers A' and B' the substitution rate being the same for layers A and B.

The Basal (100) sulfur layers consist in "discrete" S_2 dumbells (*i.e.* d_{S-S} ~ 2.10 Å), all perpendicularly oriented and well separated to each other by ca. 3.15 Å. Due to the *C*-centering, two successive sulfur layers are shifted by a **a/2 + b/2** vector. These layers are depicted in **Fig. 1b** (left) with sulfur atoms represented in yellow (hereafter labeled as layer A) and orange (hereafter labeled as layer B) for x-heights of 0 and ½, respectively.

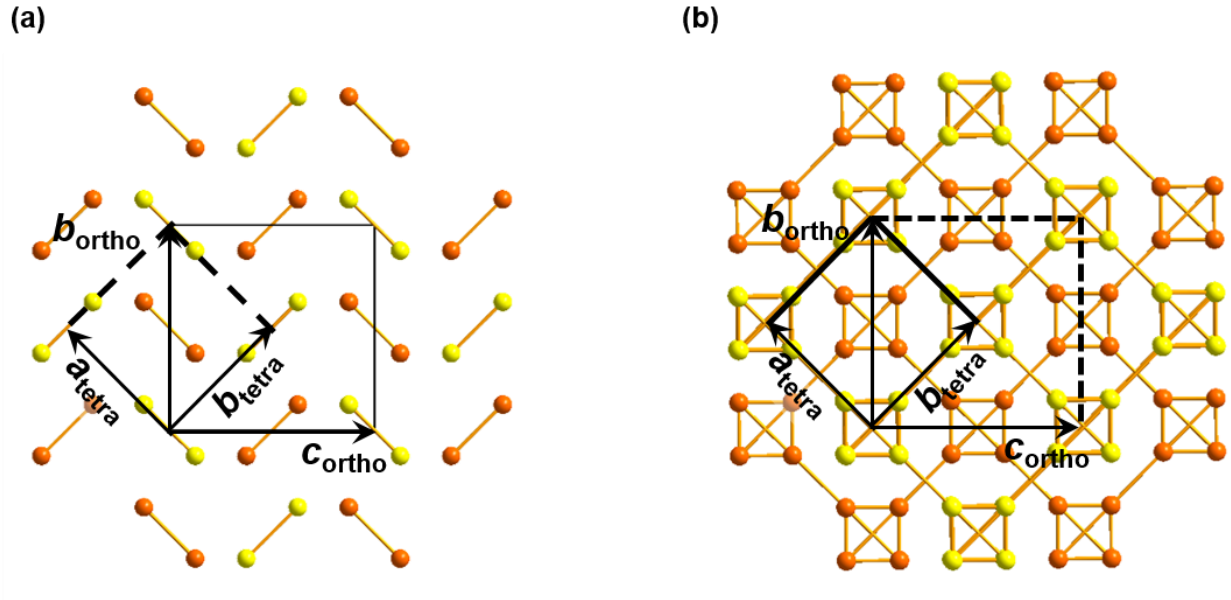

Figure 2. Sulfur layers in the structure of $Ln_2O_2S_2$ (*Ln* = La, Pr, Nd) materials (a) according to Ostoréro et Leblanc [11] (*Cmce* SG) viewed along the [100] axis, and (b) according to Ballestracci [12] (*I4/mmm* SG, occupancy rate of S site of 0.5) viewed along the [001] axis. Sulfur atoms are represented as full circles colored either in yellow (x or z-height = 0 in *Cmce* or *I4/mmm*, respectively) or orange (x or z-height = 1/2 in *Cmce* and *I4/mmm*, respectively). This color code for $(S_2)^{2-}$ dimers corresponds to layer A (yellow) and layer B (orange) in Figure 1b. Black arrows indicate lattice vectors of the orthorhombic *Cmce* model and the tetragonal *I4/mmm* model.

The tetragonal structure model proposed by Ballestracci [12] (*I4/mmm* space group; *Z*=2; one unique and different atomic positions for *Ln*, O and S atoms, respectively) derives from the orthorhombic setting by applying a transformation matrix (001, 110, -110) for the I4/mmm-to-Cmce model without origin shift. Going from the orthorhombic to the tetragonal setting, i.e. from the Ostoréro [11] to the Ballestracci model [12], the main change in terms of atomic arrangement concerns the sulfur layers. The intrinsic symmetry of $[Ln_2O_2]^{2+}$ layers and their long range ordering along the stacking axis in the *Cmce* SG are indeed compatible with the *I4/mmm* SG within the cell parameter standard deviations. In contrast, the tetragonal symmetry brings about different situations concerning the orientation of $(S_2)^{2-}$ dimers (see **Fig. 2**). The main consequence brought by a 4-fold axis is the replacement of each isolated (S_2) dimer (**Fig. 2a**) in the orthorhombic model by square crosses of S_2 dimers in the tetragonal model where each sulfur atom site is half occupied (see **Fig. 2b**). These square crosses are interconnected to form an infinite sulfur sub-lattice. Such a straightforward view of the $Ln_2O_2S_2$ structures must be however rejected as its [S_4] squares impose too short S−S distances of ~1.50 Å. In fact, Ballestracci [12] interpreted this tetragonal model as the result of a disordered stacking of $(S_2)^{2-}$ arrays along the stacking axis (See **Fig. 1)**. Indeed, four types of S layers would exist in the material, A and A', and B and B', A' and B' deriving from A and B layers via a 90° rotation perpendicular to the layers. Unlike the *Cmce* model, sulfur layers A and A', and B and B' are stacked in a random manner and each orientation type accounts for exactly 50% of an overall percentage.

As a whole, the two models proposed respectively by Ostoréro et al. [11] and Ballestracci [12] are only two types of sulfurs layers, layer A and layer B, displayed in **Figure 1b** (left) and linked by symmetry elements of the orthorhombic *Cmce* space group. Layer B follows from layer A by a

simple in-plane translation, i.e. a **b/2** translation, and the sequence layer A-layer B is repeated *ad infinitum*. In contrast, Ballestracci [12] refined the $La_2O_2S_2$ structure in the tetragonal *I4/mmm* space group. Then, two sulfur variants to layers A and layers B have to be considered. They are labelled layers A' and layers B' hereafter and are depicted in **Figure 1b** (right). They derive from layers A and B by a 90° rotation along the stacking axis. Formally, layers A' and B' are the mirror images of layers A and B, and each S_2 dumbbell is consequently rotated by 90° going from layer A and B to A' and B' with a gravity center that remains unchanged. To some extent, layer B' (A') can be also regarded as a copy of layer A (B) via a b/2 translation of the orthorhombic cell. Whatever, as layers A and A', and layers B and B' are equiprobable in the Ballestracci model, the tetragonal symmetry is naturally preferred to the orthorhombic one, the basal parameters of the orthorhombic cells being identical within the estimated standard deviation.

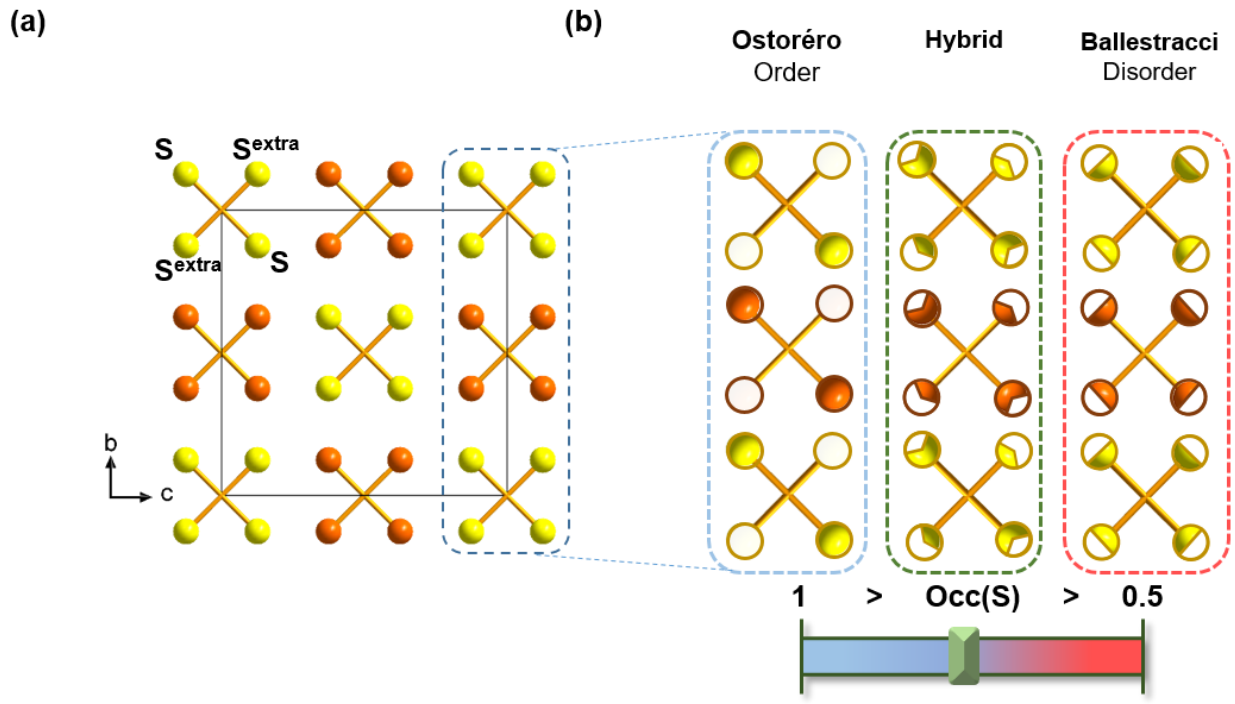

Figure 3. (a) Representation of the sulfur layers viewed along the [100] axis in the revised *Cmce* model where an additional sulfur site "S^{extra}" was added. Site occupancy for the additional sulfur is constrained by: $Occ(S^{extra}) = 1 - Occ(S)$. (b) Zoom showing a comparison of the sulfur site occupations in the Ostoréro, Ballestracci and hybrid models.

Between these two extreme situations, an intermediate one may also be considered. Indeed, the long-range ordering of $(S_2)^{2-}$ orientation is surely present as evidenced previously by detailed single-crystal XRD analyses, [11] but stacking faults may induce other types of $(S_2)^{2-}$ orientations. For a better description of the $Ln_2O_2S_2$ structure, one must develop therefore a structure model representing such a coexistence of long-range ordering and stacking faults.

Therefore, we herein propose a "hybrid" model that describes the situation halfway between the completely ordered stacking proposed by Ostoréro et Leblanc and the random stacking proposed by Ballestracci. One of the simplest way for that purpose is to add an extra sulfur atomic position (S^{extra}), in supplement to the regular S site, to the original *Cmce* structure model (See **Figure3**). It may seem that the new model simply mimics the S_4 square crosses observed in the tetragonal setting (see **Table S2** for comparison of structure parameters). In fact, the revised *Cmce* model can independently tune the occupancy of each S_2 dimers in the S_4 square cross unit, unlike the original *Cmce* and *I*4*/mmm* models that supposed only single sites for sulfur atoms. As a consequence, the "hybrid" model can reproduce both extreme situations concerning $(S_2)^{2-}$ orientation order (**Figure 3b)**. When occupancy rates are 100% for S site and 0% for S^{extra} site, it becomes equivalent to the "perfectly ordered" original *Cmce* model while the completely disordered *I*4*/mmm* model can be reproduced with an occupancy rate of 50% for both S and S^{extra} sites. When the occupancy rate for the S site takes a value between 100-50% (or 0-50% for S^{extra} site), the "hybrid" model represents the situation where A and A', and B and B' layers (two

different types of $(S_2)^{2-}$ orientations not symmetry related by the orthorhombic space group) coexist and are present as stacking faults. In other words, the similarity to each extreme situation can be parametrized using occupancy rates for the sulfur sites Occ(S) and Occ(S^{extra}):

$$0 \leq \left| Occ(S) - Occ(S^{extra}) \right| \leq 1$$

When it equals 0, $(S_2)^{2-}$ orientation is completely disordered along stacking axis while $(S_2)^{2-}$ orientation type is uniformed when it takes value of 1. It must be noted that the proposed "hybrid" model cannot structurally speaking clarify the type of disorder involved in the crystallites. It cannot for instance distinguish between a situation where A and A' layers, and B and B' layers are randomly distributed and a situation where small micro domains built upon A and B layers or A' and B' layers would also randomly alternate along the stacking axis.

As a preliminary step, $La_2O_2S_2$ sample prepared by high-temperature ceramic synthesis (i.e. $La_2O_2S_2$-1) was used for validation of our new structural model. Firstly, its powder XRD pattern recorded at room temperature was tentatively subjected to Rietveld refinements with both models (See **Table S2** for the refined structure parameters). Refinement using the structural model proposed by Ballestracci [12] (*I4/mmm* space group) gave cell parameters of a = 4.1968(5) Å, and c = 13.2067(2) Å (**Fig. 4a**), while the refinement using the model reported by Ostoréro et Leblanc (*Cmce* space group) led to a = 13.207(5) Å, b = 5.9351(2) Å, and c = 5.9353(2) Å (**Fig. 4b**). Apparently, *I4/mmm* space group proposed by Ballestracci [12] could not explain the small peak around $2\theta = 33.7°$ implying the presence of lower symmetry for the $La_2O_2S_2$ structure. At the opposite, that peak could be indexed as *021* reflection of the *Cmce* space group proposed by Ostoréro et Leblanc [11]. However as shown in **Fig. 4b** this model is also introducing other additional peaks such as *112* and *221* reflections whose intensity was overestimated compared to the experimental data.

This observation supports our hypothesis that the real structure of $La_2O_2S_2$ is an intermediate between the Ostoréro and Ballestracci's models. Refinement carried out using our "hybrid" model led to *a*, *b* and *c* cell parameters of 13.2065(4) Å, 5.9351(2) Å, and 5.9353(2) Å, with reliability factors of $\chi^2 = 1.58$ and $R_{obs} = 2.04$. Refined occupancy of S (Site 1) and S^{extra} (Site 2) was 67(3)% and 33(3)%, respectively (**Table S2,** See **Fig. 4c** for fitting). Now the "hybrid" model properly represents the small additional peaks that were ignored in *I*4/*mmm* model but exaggerated in the original *Cmce* model. Let us notice that the insertion of a second S atom in the hybrid model does not induce significant changes in the coordination polyhedra of La atoms. La−S and La−S^{extra} distances remain indeed identical within the esd (3.16(4) Å vs. 3.09(6) Å, see **Table S5**). Formally, the propensity of $La_2O_2S_2$ structure to exhibit stacking faults was probed by ab initio calculations [16] carried out on an orthorhombic 2a×b×c supercell (48 atoms). A total energy cost lower than 2 meV was calculated going from an ABAB to an ABA'B or ABA'B' stackings of S-layers. This clearly suggests that defects are likely to occur in $La_2O_2S_2$.

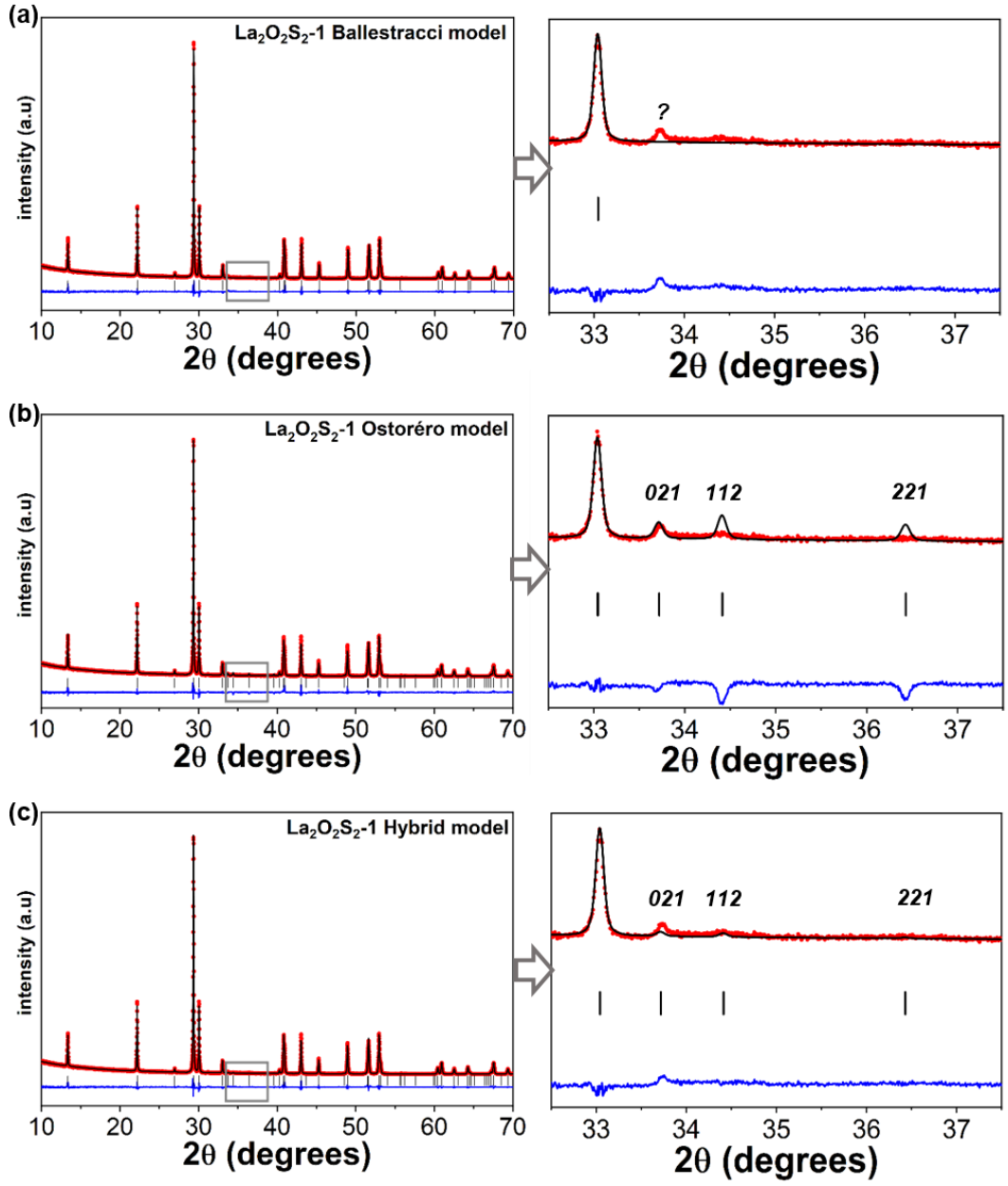

Figure 4. Rietveld refinements of $La_2O_2S_2$-1 with the Ballestracci model (*I4/mmm*) (a), the Ostorero model (*Cmce* – one S site) (b), and the hybrid model (*Cmce* – two S sites) (c). The left panels display the full diagrams while the right panels display zoom-in zooms in the 32.5-37.5 2θ region. The black, red and blue curves represent respectively the experimental, calculated and difference diagrams. The refined Bragg positions are represented by gray vertical lines.

The hybrid model was refined also using the XRD pattern of $La_2O_2S_2$-2 (**Fig. 5**). This led to *a*, *b* and *c* cell parameters of 13.223(10) Å, 5.9382(2) Å, and 5.9381(2) Å, with reliability factors of χ^2 = 1.90 and R_{obs} = 2.08, and occupancy rates of S and S^{extra} sites of 76(5)% and 24(5)%, respectively (see **Table S3**). This suggests that the extent of disorder in stacking of different orientation types may vary depending on the chosen synthesis conditions.

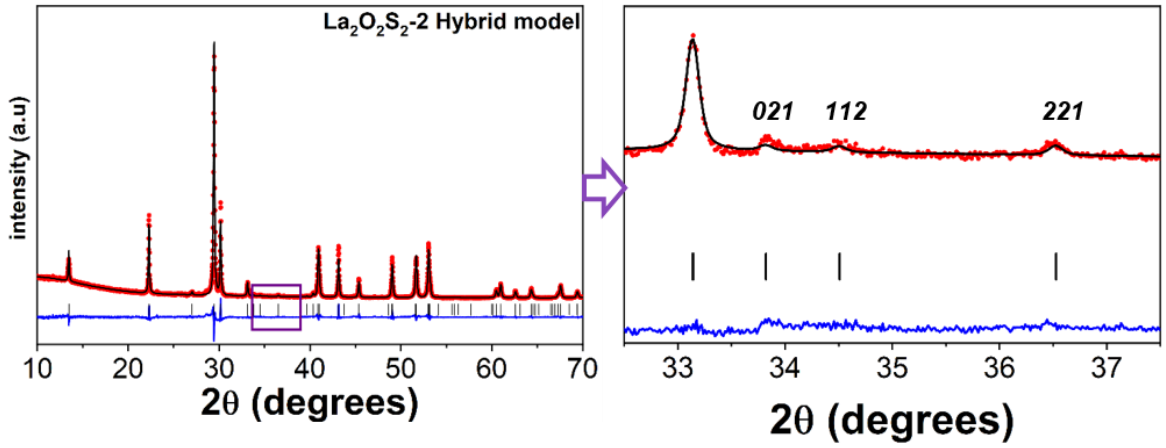

Figure 5. Rietveld refinement of the $La_2O_2S_2$-2 X-ray powder pattern using the hybrid model. The left panels display the full diagram while the right panels display a zoom-in in the 32.5-37.5 2θ region (grey rectangle). The black, red and blue curves represent respectively the experimental, calculated and difference diagrams. The refined Bragg positions are represented by gray vertical lines.

$La_2O_2S_2$-3 and $La_2O_2S_2$-4 samples prepared via soft-chemical routes at low-temperature (*T* = 200 °C) displayed relatively broad and small XRD peaks possibly due to lower crystallinity of the samples (**Fig. S2**). These broad features rendered the reflections characteristic of the orthorhombic space group difficult to be spotted. Nevertheless, both XRD patterns were equally fitted well using the hybrid model of $La_2O_2S_2$.

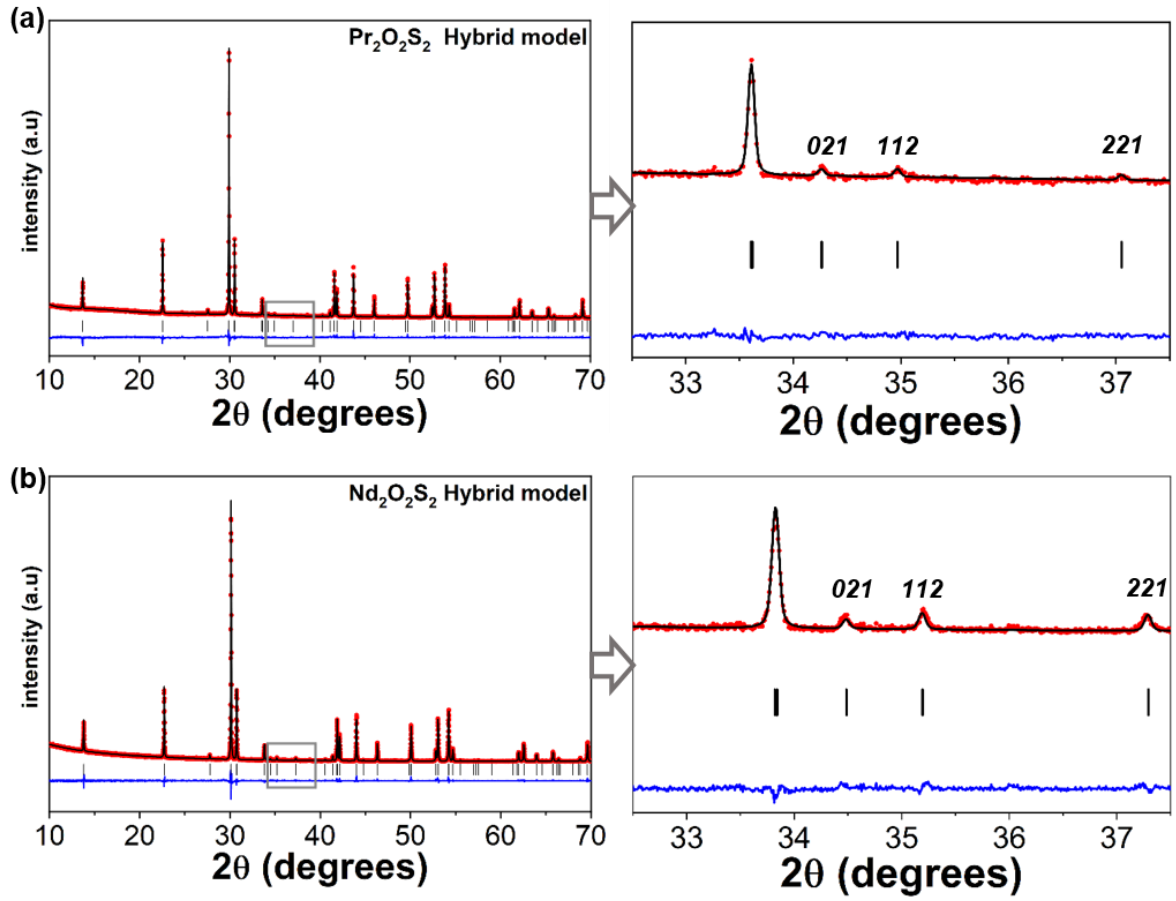

Figure 6. In the left panels, Rietveld refinements with the hybrid model of $Pr_2O_2S_2$-1 (a) and $Nd_2O_2S_2$-1 (b). The black, red, and blue curves represent in order the calculated, experimental, and difference plots between the two. Bragg positions represented by vertical lines are in gray. In the enlarged panels on the right, the green and red colors define respectively the calculated diagrams with the hybrid model and the experimental diagrams. The calculated plots are superimposed on the experimental plot in red. The difference curve (in green) between the experimental and calculated diagrams is located near the x-axis. The Bragg positions given by vertical lines inform on the existence of peaks at reflections 021, 112 and 221.

In a similar way, the XRD pattern of $Pr_2O_2S_2$ was better explained by the hybrid model (*Cmce* space group) that yielded a proper representation of its 021, 112 and 221 reflections (**Fig.6a**). The refined occupancy rates were 76(3)% for S and 24(3)% for S^{extra} atomic sites, and the refined Pr−S and Pr−S^{extra} distances remained identical within the esd. (see **Tables S4 and S5**). $Nd_2O_2S_2$ displayed 021, 112 and 221 reflections more pronounced than its La and Pr homologues (**Fig.6b**). Accordingly, its occupancy rates were 86(2)% and 14(2)% for S and S^{extra} atomic sites (see **Tables S4)**. This indicates a less disordered stacking of disulfide layers in $Nd_2O_2S_2$-1 than in $Pr_2O_2S_2$-1 and $La_2O_2S_2$-1. As a whole, the occupancy of the S^{extra} site for $Ln_2O_2S_2$ materials prepared in similar conditions increased along the $Nd_2O_2S_2$ < $Pr_2O_2S_2$ < $La_2O_2S_2$ sequence, suggesting that the bigger the trivalent lanthanide, the higher its propensity to create irregular stacking of $(S_2)^{2-}$ layers. The interatomic distances in $La_2O_2S_2$-1, $Pr_2O_2S_2$ and $Nd_2O_2S_2$ are summarized in **Table S5**. It may be observed that *Ln*−O and La−S distances decrease on going from La to Pr and Nd, in direct relation with the lowering of the ionic radii of Ln^{3+} cations (1.30 Å, 1.266 Å and 1.24 Å for La^{3+}, Pr^{3+} and Nd^{3+}). The thickness of the $[Ln_2O_2]^{2+}$ slabs and the inter-slab distances decrease along the sequence. [17] Conversely the S−S distances of the dimers remain identical within the estimated standard deviations whatever the Ln^{3+} cations.

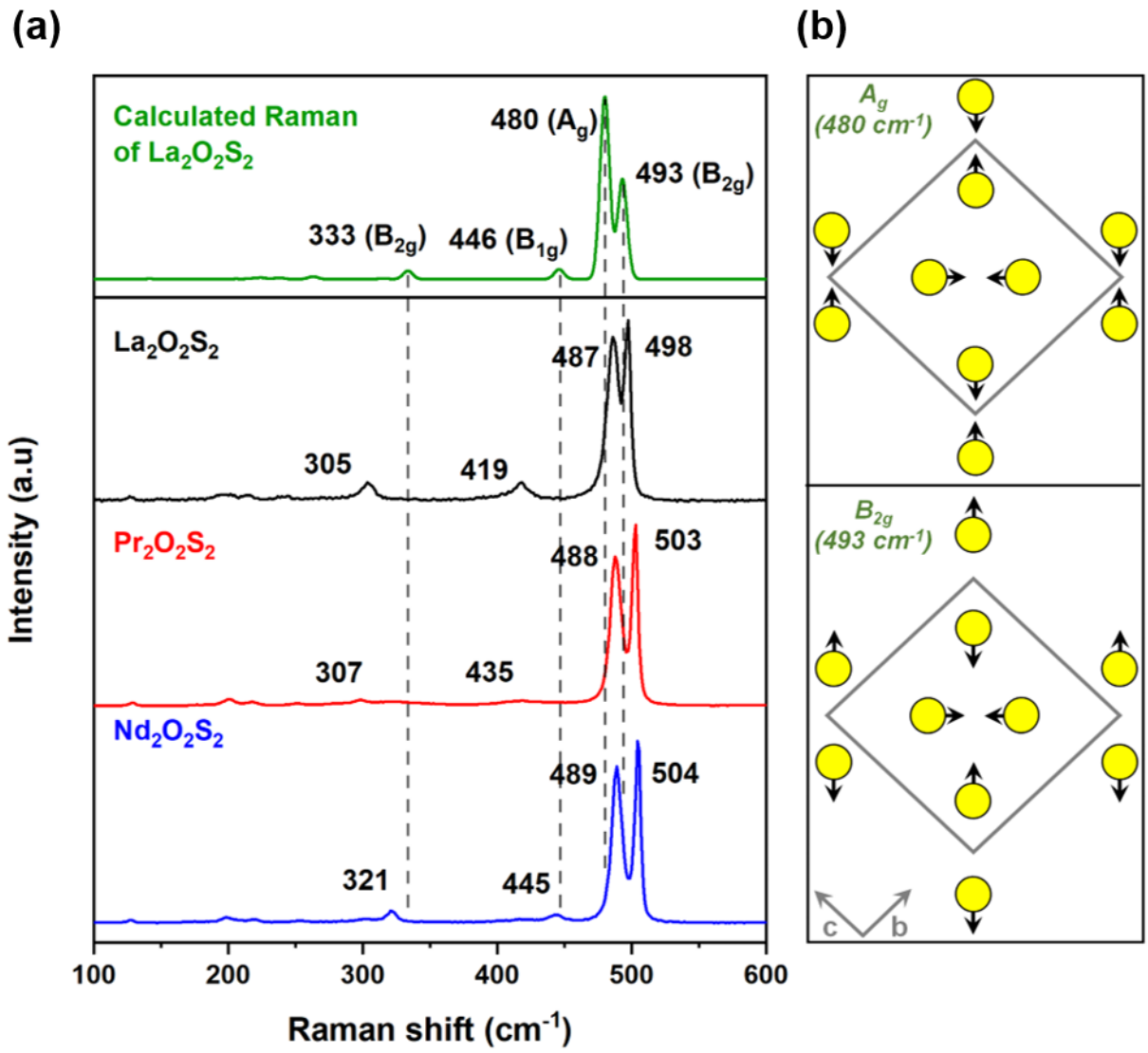

Figure 7. (a) Observed Raman spectra of $La_2O_2S_2$, $Pr_2O_2S_2$ and $Nd_2O_2S_2$ and calculated Raman spectra of $La_2O_2S_2$. (b) Symmetric (480 cm^{-1}) (the two S_2 dimers of a S-layers vibrate in phase) and asymmetric (493 cm^{-1}) (the two S_2 dimers of a S-layers vibrate out of phase) stretching S−S vibrations within an (S_2) layers.

Raman spectra were collected on samples $La_2O_2S_2$-1, $Pr_2O_2S_2$-1and $Nd_2O_2S_2$-1 (**Fig. 7a**). In the 100-600 cm^{-1} domain, the three spectra turn out to be very similar with a prominent contribution of the S−S dimers giving rise to two bands peaking at 487 and 498 cm^{-1}, 488 and

503 cm^{-1} and 489 and 504 cm^{-1} for La, Pr and Nd variants, respectively. Steudel law ($d_{(S-S)}^{2-}$ (Å) = 2.57 – 9.47x10^{-4} $\upsilon_{(S-S)}$ (cm^{-1})) [18] relates frequencies of respective bands to S−S distances of 2.109 and 2.098 Å for La, 2.108 and 2.094 Å for Pr, and 2.107 and 2.093 Å for Nd variants. These values were comparable to those calculated from the refined "hybrid" structure model with *Cmce* space group: 2.12(8) and 2.11(10) for La, 2.09(3) and 2.07(8) Å for Pr, and 2.123(2) and 2.09(7) Å for Nd (**Table S5**). Such agreements tempt us to have an intuitive conjecture that the two observed bands originate from two different S−S bond lengths as expected in the "hybrid" model. However, if 2D packing of $(S_2)^{2-}$ dimers gives rise to two energetically distinct vibrational modes, it is also possible to observe such a doublet Raman band from layers without variety in S−S bond lengths. To answer this, ab initio calculations on the $La_2O_2S_2$ compound were carried out. Firstly, the Ostoréro's model in *Cmce* space group was subject to geometry relaxation, followed by the simulation of its Raman spectra (**Fig. 7a**). Raman bands calculated at 480 (A_g) and 493 (B_{2g}) cm^{-1} were assigned unambiguously to symmetric and asymmetric stretching S−S vibrations coupled with breathing/rocking in a $[S_2]$ layer as displayed in **Fig. 7b**. Namely, four S−S dimers exist in the C-face centered orthorhombic cell, *i.e.* two dimers in the primitive cell. Consequently, two signals are expected corresponding to in-phase and out-of-phase vibrations of the two 0-D vibrators. Let us notice that calculations carried out on a faulted $La_2O_2S_2$ material, *i.e.* calculations with a supercell containing one S layer over four rotated by 90° along the a-axis of the ideal *Cmce* structure, do not modify the simulated Raman spectrum and the position of the S−S bonds. Clearly, this signifies that no direct vibrational interaction exists between two adjacent S layers separated by a $[La_2O_2]$ fluorine block. This fully agrees with the observation that two bands are perceived for $La_2O_2S_2$-1, $Pr_2O_2S_2$-1 and $Nd_2O_2S_2$-1 whatever the space group (i.e. *Cmce* and *I*4*/mmm*), the model (hybrid or not), and the occupancy

rates of S and S^{extra}. At this stage, it may appear difficult to discriminate between a block model with successive micro-domains rotated by 90° and a random rotational disorder (rotation of 90° of the S_2 dimers along the stacking axis in A and A', and B and B' layers). Nevertheless, Raman spectra clearly evidence the equivalence of all sulfur layers, i.e. layers well organized in the basal plane built upon S_2 dumbbells as displayed in **Fig. 1b** where all S sites are fully occupied (at the defect detection limit). On the crystal point of view, these layers are all related to each other via the symmetry operators of the *Cmce* space group plus a pseudo 4 fold axis perpendicular to the a axis due to the propensity of infinite 0-height and ½-height S layers to rotate by 90° for a very low energy cost. For information, observed (calculated) bands peaking at 419 (445 (B_{3g}) and 446 (B_{1g})), 305 (314 (A_g), 315 (B_{1g}) and 333 (B_{2g})) cm^{-1} in $La_2O_2S_2$-1 are mainly related to oxygen motions.

Kubelka-Munk transformed diffuse reflection spectra of $La_2O_2S_2$-1, $Pr_2O_2S_2$ and $Nd_2O_2S_2$ are depicted in **Fig. 8a**. All of them are characterized by a steep absorption threshold 2.68 eV, 2.33 eV and 2.54 eV for the La, Pr and Nd phases preceded by a shoulder at ca. 2.56, 2.36 and 2.38 eV, respectively. For $Pr_2O_2S_2$ and $Nd_2O_2S_2$, sharp absorption peaks associated to f-f transitions are also observed at lower energies with a much lesser intensity as expected due to their Laporte-forbidden character. $La_2O_2S_2$ is yellow, $Pr_2O_2S_2$ green pale and $Nd_2O_2S_2$ olive green.

Band structure calculations were carried out on $La_2O_2S_2$ using the model of Ostoréro et al. (*Cmce* SG,). The total Density of States (DOS) and the projected DOS on the different atoms are represented in **Figure 9a**. The calculation reveals as expected an insulating compound with a gap slightly lower than 3 eV in good agreement with the reflection spectra. Around the Fermi level the conduction band (CB) minimum and valence band (VB) maximum are built upon S p orbitals. The Lanthanum d states lie well above the Fermi level E_F (4.5 eV to 10 eV) while the p

level of oxygen lies within the conduction band between -2 and -5 eV. Due to the formation of the S−S bond the p bands of S are split from either side of the Fermi levels in (σ_{S-S}, π_{S-S}, π^*_{S-S}) and σ^*_{S-S} sub bands. The σ^*_{S-S} block is ranging from +3 to 4.5 eV and constitutes the conduction band while the valence band is built at the top of π^*_{S-S} states. The **Figure 9b** gives a sketch of the band structure. The electronic density calculated for the states at the valence band maximum and the conduction band minimum are also represented on this figure. The formation of antibonding σ^*_{S-S}, and π^*_{S-S} bonds are clearly visible. From the calculated $\varepsilon_2(E)$ curve given in **Fig. 8b**, the absorptions at 2.56 eV and 2.68 eV might be assigned to a $\pi^*_{S-S} \rightarrow \sigma^*_{S-S}$ and a $\pi^*_{S-S} \rightarrow$ 5d-La transitions. The former is especially active for electric dipoles orientated within the (100) plan ($\varepsilon_{2yy}(E)$ and $\varepsilon_{2zz}(E)$), while the later contributes to ($\varepsilon_{2xx}E$).

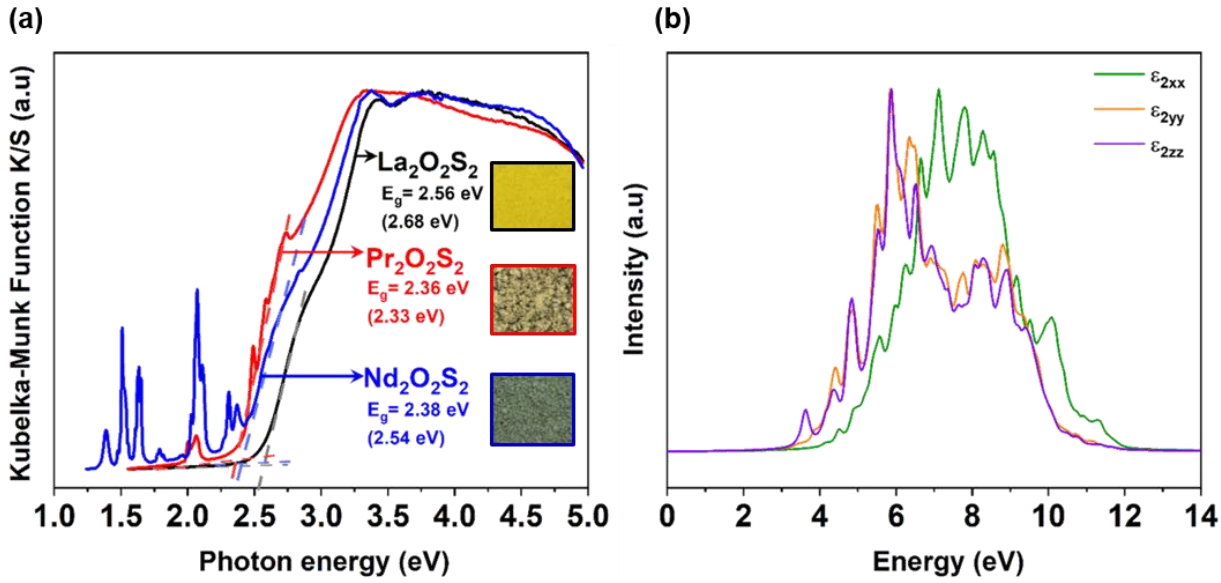

Fig. 8. (a) Kubelka-Munk transformed reflectance spectra of $La_2O_2S_2$-1, $Pr_2O_2S_2$ and $Nd_2O_2S_2$. (b) Imaginary part of the dielectric function of $La_2O_2S_2$.

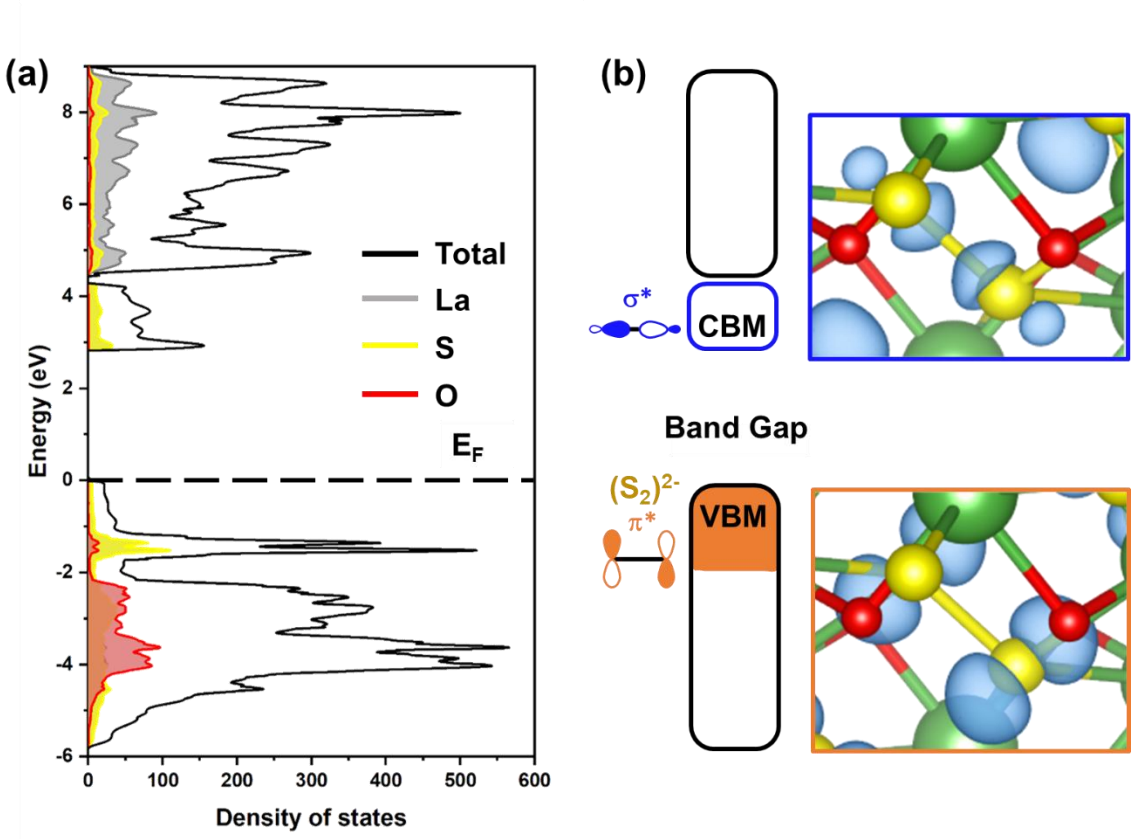

Fig. 9. (a) Density of states with atomic contributions of La, O and S. (b) Sketch of the calculated electronic structure of $La_2O_2S_2$ with the occupied π^*_{S-S} and empty σ^*_{S-S} levels, respectively. The left panels represent the isosurfaces of electronic density of the VBM and CBM and evidence the S−S antibonding states.

CONCLUSION

So far, two structural models were reported in the literature to account for the crystal structure of $Ln_2O_2S_2$ (*Ln* = La, Pr, Nd) materials: one in orthorhombic symmetry shows a full occupancy of the S site, and another one in tetragonal symmetry shows a half occupancy of the S site. The difference between them resides in the sulfur layers that are not long range ordered along the stacking axis in the tetragonal cell. We evidence that the right model consists in an intermediate structure between the one proposed by Ostoréro et al. [11] (*Cmce* SG) and Ballestracci [12] (*I*4*/mmm*). Formally, all collected XRD patterns can be refined in the orthorhombic structure using the *Cmce* and two possible positions for sulfur atoms. Thus, the Ostoréro et al. [11] (*Cmce* SG) and Ballestracci [12] (*I*4*/mmm*) models can be reconciled, a tetragonal symmetry being recovered if the two sulfur atoms of the intermediate model are identically half occupied. Formally, the occupancy of the S and S^{extra} atoms in the new model turns to be very dependent of the lanthanide but also of the synthesis conditions. This explains the discrepancy in the models reported so far in the literature.

ASSOCIATED CONTENT

Supporting Information.

The following files are available free of charge.

The supporting information file contains some computational details, a description of the chemical environment in the $Ln_2O_2S_2$ compounds (Ln=La, Pr and Nd), a table summarizing the structural parameters reported for $Ln_2O_2S_2$ in the literature, and some tables and figures about the different Rietveld refinements performed on the $Ln_2O_2S_2$ compounds (Ln=La, Pr and Nd).

AUTHOR INFORMATION

Corresponding Author

* Laurent.cario@cnrs-imn.fr; Stephane.jobic@cnrs-imn.fr

Author Contributions

The manuscript was written through contributions of all authors. All authors have given approval to the final version of the manuscript.

Notes

The authors declare no competing financial interests.

ACKNOWLEDGMENT

The PhD grant of L-B M. was financially supported by the CNRS and the region Pays-de-la-Loire.

REFERENCES

(1) Chung, I.; Kanatzidis, M. G. Metal Chalcogenides: A Rich Source of Nonlinear Optical Materials. *Chem. Mater.* **2014**, *26* (1), 849–869. https://doi.org/10.1021/cm401737s.

(2) Santelli, J.; Lechevallier, S.; Calise, D.; Marsal, D.; Siegfried, A.; Vincent, M.; Martinez, C.; Cussac, D.; Mauricot, R.; Verelst, M. Multimodal Gadolinium Oxysulfide Nanoparticles for Bioimaging: A Comprehensive Biodistribution, Elimination and Toxicological Study. *Acta Biomaterialia* **2020**, *108*, 261–272. https://doi.org/10.1016/j.actbio.2020.03.013.

(3) Mathew, M. E.; Mohan, J. C.; Manzoor, K.; Nair, S. V.; Tamura, H.; Jayakumar, R. Folate Conjugated Carboxymethyl Chitosan–Manganese Doped Zinc Sulphide Nanoparticles for

Targeted Drug Delivery and Imaging of Cancer Cells. *Carbohydrate Polymers* **2010**, *80* (2), 442–448. https://doi.org/10.1016/j.carbpol.2009.11.047.

(4) Yu, Y.; Cagnoni, M.; Cojocaru-Mirédin, O.; Wuttig, M. Chalcogenide Thermoelectrics Empowered by an Unconventional Bonding Mechanism. *Advanced Functional Materials* **2020**, *30* (8), 1904862. https://doi.org/10.1002/adfm.201904862.

(5) Wang, Q.; Nakabayashi, M.; Hisatomi, T.; Sun, S.; Akiyama, S.; Wang, Z.; Pan, Z.; Xiao, X.; Watanabe, T.; Yamada, T.; Shibata, N.; Takata, T.; Domen, K. Oxysulfide Photocatalyst for Visible-Light-Driven Overall Water Splitting. *Nature Materials* **2019**, *18*, 827–832. https://doi.org/10.1038/s41563-019-0399-z.

(6) Sasaki, S.; Kriener, M.; Segawa, K.; Yada, K.; Tanaka, Y.; Sato, M.; Ando, Y. Topological Superconductivity in $Cu_xBi_2Se_3$. *Phys. Rev. Lett.* **2011**, *107* (21), 217001. https://doi.org/10.1103/PhysRevLett.107.217001.

(7) Hu, C.; Ding, L.; Gordon, K. N.; Ghosh, B.; Tien, H.-J.; Li, H.; Linn, A. G.; Lien, S.-W.; Huang, C.-Y.; Mackey, S.; Liu, J.; Reddy, P. V. S.; Singh, B.; Agarwal, A.; Bansil, A.; Song, M.; Li, D.; Xu, S.-Y.; Lin, H.; Cao, H.; Chang, T.-R.; Dessau, D.; Ni, N. Realization of an Intrinsic Ferromagnetic Topological State in $MnBi_8Te_{13}$. *Science Advances* **2020**, *6* (30), eaba4275. https://doi.org/10.1126/sciadv.aba4275.

(8) Caron, J. M.; Neilson, J. R.; Miller, D. C.; Llobet, A.; McQueen, T. M. Iron Displacements and Magnetoelastic Coupling in the Antiferromagnetic Spin-Ladder Compound $BaFe_2Se_3$. *Phys. Rev. B* **2011**, *84* (18), 180409. https://doi.org/10.1103/PhysRevB.84.180409.

(9) Sasaki, S.; Caldes, M. T.; Guillot-Deudon, C.; Braems, I.; Steciuk, G.; Palatinus, L.; Gautron, E.; Frapper, G.; Janod, E.; Corraze, B.; Jobic, S.; Cario, L. Design of Metastable Oxychalcogenide Phases by Topochemical (de)Intercalation of Sulfur in $La_2O_2S_2$. *Nat Commun* **2021**, *12* (1), 3605. https://doi.org/10.1038/s41467-021-23677-w.

(10) Sasaki, S.; Driss, D.; Grange, E.; Mevellec, J.-Y.; Caldes, M. T.; Guillot-Deudon, C.; Cadars, S.; Corraze, B.; Janod, E.; Jobic, S.; Cario, L. A Topochemical Approach to Synthesize Layered Materials Based on the Redox Reactivity of Anionic Chalcogen Dimers. *Angewandte Chemie* **2018**, *130* (41), 13806–13811. https://doi.org/10.1002/ange.201807927.

(11) Ostoréro, J.; Leblanc, M. Room-Temperature Structure of $La_2O_2S_2$. *Acta Crystallographica Section C* **1990**, *46* (8), 1376–1378. https://doi.org/10.1107/S0108270189013375.

(12) Ballestracci, R. Structure cristalline des oxydisulfures de terres rares $Ln_2O_2S_2$. *Materials Research Bulletin* **1967**, *2* (7), 473–479. https://doi.org/10.1016/0025-5408(67)90068-2.

(13) Dusek, M.; Petricek, V.; Palatinus, L. Introduction to JANA2006. *Acta Cryst A* **2006**, *62* (a1), 46–46. https://doi.org/10.1107/S0108767306099089.

(14) Hafner, J. Ab-Initio Simulations of Materials Using VASP: Density-Functional Theory and Beyond. *Journal of Computational Chemistry* **2008**, *29* (13), 2044–2078. https://doi.org/10.1002/jcc.21057.

(15) Grenier, B.; Ballou, R. Crystallography: Symmetry Groups and Group Representations. *EPJ Web of Conferences* **2012**, *22*, 00006. https://doi.org/10.1051/epjconf/20122200006.

(16) Coelho, A. A.; Evans, J. S. O.; Lewis, J. W. Averaging the Intensity of Many-Layered Structures for Accurate Stacking-Fault Analysis Using Rietveld Refinement. *J Appl Cryst* **2016**, *49* (5), 1740–1749. https://doi.org/10.1107/S1600576716013066.

(17) Pauwels, D. Cristallochimie des composés de terres rares à anions mixtes. Propriétés d'absorption uv-visible, Université Sciences et Technologies - Bordeaux I, **2003**. https://tel.archives-ouvertes.fr/tel-00011917.

(18) Steudel, R.; Chivers, T. The Role of Polysulfide Dianions and Radical Anions in the Chemical, Physical and Biological Sciences, Including Sulfur-Based Batteries. *Chemical Society Reviews* **2019**, *48* (12), 3279–3319. https://doi.org/10.1039/C8CS00826D.

SYNOPSIS (Word Style "SN_Synopsis_TOC").

The exact structure of $La_2O_2S_2$ material and its Pr and Nd derivatives is still subject to debate. The two structural models known so far report either an ordered or a fully disordered sulfur dimers $(S_2)^{2-}$ arrays sandwiched by $[La_2O_2]$ layers. In this study, we revisit the crystal structure of $Ln_2O_2S_2$ (*Ln*= La, Pr, and Nd) materials and propose an alternative model that reconciles the two points of view.

Graphic TOC (8.25 cm by 4.45 cm)

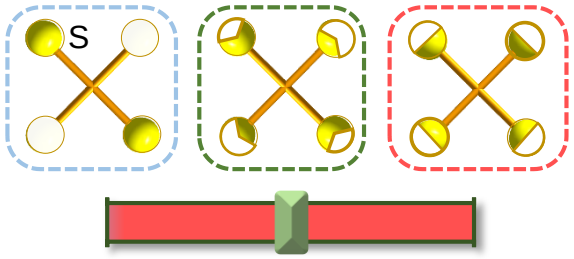

Order **New model** Disorder